

COSMIC VELOCITY FIELD RECONSTRUCTION USING AI

ZIYONG WU¹, ZHENYU ZHANG¹, SHUYANG PAN¹, HAITAO MIAO¹, XIAOLIN LUO¹, XIN WANG^{1†}, CRISTIANO G. SABIU^{2,3}, JAIME FORERO-ROMERO⁴, YANG WANG^{1‡}, XIAO-DONG LI^{1*}
School of Physics and Astronomy, Sun Yat-Sen University, Guangzhou 510297, P. R. China¹
Department of Astronomy, Yonsei University, 50 Yonsei-ro, Seoul 03722, Korea²
Natural Science Research Institute, University of Seoul, 163 Seoulsiripdaero, Dongdaemun-gu, Seoul, 02504, Republic of Korea³ and
Departamento de Física, Universidad de los Andes, Cra. 1 No. 18A-10 Edificio Ip, CP 111711, Bogotá, Colombia⁴

Draft version May 21, 2021

ABSTRACT

We develop a deep learning technique to infer the non-linear velocity field from the dark matter density field. The deep learning architecture we use is an “U-net” style convolutional neural network, which consists of 15 convolution layers and 2 deconvolution layers. This setup maps the 3-dimensional density field of 32^3 -voxels to the 3-dimensional velocity or momentum fields of 20^3 -voxels. Through the analysis of the dark matter simulation with a resolution of $2h^{-1}\text{Mpc}$, we find that the network can predict the non-linearity, complexity and vorticity of the velocity and momentum fields, as well as the power spectra of their value, divergence and vorticity and its prediction accuracy reaches the range of $k \simeq 1.4 h\text{Mpc}^{-1}$ with a relative error ranging from 1% to $\lesssim 10\%$. A simple comparison shows that neural networks may have an overwhelming advantage over perturbation theory in the reconstruction of velocity or momentum fields.

Subject headings: Cosmology:

1. INTRODUCTION

The large-scale structure (LSS) of the Universe is a key observational probe to study the physics of dark matter, dark energy, gravity and cosmic neutrinos. In the next 10 years, stage IV surveys, including DESI¹, EUCLID², LSST³, WFIRST⁴, and CSST, will begin to map out an unprecedented large volume of the Universe with extraordinary precision. It is of critical importance to have statistical tools that can reliably extract the physical information in the LSS data.

The peculiar velocities of the galaxies, sourced by the “initial” inhomogeneities, is an excellent probe for the physics of the LSS, enabling us to better study or measure such quantities as the redshift space distortions Kaiser (1987); Jackson (1972), baryon acoustic oscillations (Eisenstein et al. 2005, 2007), the Alcock-Paczynski effect (Alcock and Paczyński 1979; Li et al. 2014; Li et al. 2015; Li et al. 2016; Ramanah et al. 2019), the cosmic web (Bardeen et al. 1986; Hahn et al. 2007; Forero-Romero et al. 2009; Hoffman et al. 2012; Forero-Romero et al. 2014; Fang et al. 2019), the kinematic Sunyaev-Zeldovich effect (Sunyaev and Zeldovich 1972, 1980), and the integrated Sachs Wolfe effect (Sachs and Wolfe 1967; Rees and Sciama 1968; Crittenden and Turok 1996).

Observationally, the measurement of the peculiar velocities is a difficult task, as it requires redshift independent determination of the distance, which is usually accomplished via distance indicators such as type Ia Supernovae (Phillips 1993; Riess et al. 1997; Raddburn-Smith et al. 2004; Turnbull et al. 2012; Mathews et al. 2016) the Tully-Fisher relation (Tully and Fisher 1977; Masters et al. 2006, 2008) and the Funda-

mental Plane relation (Dressler et al. 1987; Djorgovski and Davis 1987; Springob et al. 2007) As an alternative approach, one can “reconstruct” the cosmic velocity field from the density field based on their relationship described by theories. Here the difficulty is the complexity caused by the non-linear evolution of the structures. Numerous works have been done in this direction. For more details, one can check Nusser et al. (1991); Bernardeau (1992); Zaroubi et al. (1995); Croft and Gaztanaga (1997); Bernardeau et al. (1999); Kudlicki et al. (2000); Branchini et al. (2002); Mohayaee and Tully (2005); Lavaux et al. (2008); Bilicki and Chodorowski (2008); Kitaura et al. (2012); Wang et al. (2012); Jennings and Jennings (2015); Ata et al. (2017).

Recently machine learning algorithms, especially those based on deep neural networks, are becoming promising toolkits for the study of complex data that are difficult to be solved by traditional methods. So far, this technique have been applied to almost all sub-fields of cosmology, including weak gravitational lensing (Schmelzle et al. 2017; Gupta et al. 2018; Springer et al. 2018; Fluri et al. 2019; Jeffrey et al. 2019; Merten et al. 2019; Peel et al. 2019; Tewes et al. 2019), the cosmic microwave background (Caldeira et al. 2018; Rodriguez et al. 2018; Perraudin et al. 2019; Münchmeyer and Smith 2019; Mishra et al. 2019), the large scale structure (Ravanbakhsh et al. 2017; Lucie-Smith et al. 2018; Modi et al. 2018; Berger and Stein 2019; He et al. 2019; Lucie-Smith et al. 2019; Pfeffer et al. 2019; Ramanah et al. 2019; Tröster et al. 2019; Zhang et al. 2019; Mao et al. 2020; Pan et al. 2020), gravitational waves (Dreissigacker et al. 2019; Gebhard et al. 2019), cosmic reionization (La Plante and Ntampaka 2018; Gillet et al. 2019; Hassan et al. 2019a; Chardin et al. 2019; Hassan et al. 2019b), supernovae (Lochner et al. 2016; Moss 2018; Ishida et al. 2019; Li et al. 2019; Muthukrishna et al. 2019). For more details, one can refer to Mehta et al. (2019); Jennings et al. (2019); Carleo et al. (2019); Ntampaka et al. (2019) and the references therein.

In this paper, we apply deep learning techniques to recon-

[†]wangxin35@mail.sysu.edu.cn

[‡]wangyang23@mail.sysu.edu.cn

*lixiaod25@mail.sysu.edu.cn

¹ <https://desi.lbl.gov/>

² <http://sci.esa.int/euclid/>

³ <http://sci.esa.int/euclid/>

⁴ <https://wfirst.gsfc.nasa.gov/>

struct the velocity field from the dark matter density field. This converts the reconstruction problem to a non-linear mapping between the two fields, which is achieved via a deep neural network with a U-net style architecture. This paper is organized as follows. In section 2, we introduce the dataset and data processing methods we use. In section 3, we discuss our neural network, including the construction of our neural network, the selection of parameters and details of training, etc. Section 4 presents the main results, and section 5 represents the conclusion and discussion.

2. TRAINING AND TESTING DATASETS

The training and testing samples are generated using the COMoving Lagrangian Acceleration (COLA) code (Tassev et al. 2013). COLA computes the evolution of dark matter particles in a frame that is comoving with observers following trajectories predicted by the Lagrangian Perturbation Theory (LPT), in order to accurately deal with the small-scale structures, without sacrificing the accuracy of large scales. Being hundreds of times faster than N-body simulations, it still maintains a good accuracy from very large to highly non-linear scales.

We generate a set of 14 simulations, assuming a Λ CDM cosmology $\Omega_m = 0.31$, $\Omega_b = 0.05$, $\sigma_8 = 0.83$, $n_s = 0.96$, $H_0 = 67.77 \text{ km} \cdot \text{s}^{-1} \text{ Mpc}^{-1}$. Each of the simulation is run within a cube with a volume of $(512 h^{-1} \text{ Mpc})^3$ using 512^3 dark matter particles, having a mean separation of $1 h^{-1} \text{ Mpc}$ per dimension. The output at $z = 0$ are then used for the main part of our analysis.

The Clouding-In-Cells (CIC) algorithm is adopted for constructing the density and momentum fields from the outputs. Since the momentum has three dimensions, for each sample we need to construct three fields describing p_x , p_y and p_z , respectively. The division of the momentum and density fields then leads to three velocity fields, i.e. $v_x(\mathbf{x})$, $v_y(\mathbf{x})$ and $v_z(\mathbf{x})$ ⁵. For all fields, we choose a resolution of $(2 h^{-1} \text{ Mpc})^3$, corresponding to 256^3 voxels.

In practice, we further split the density and momentum/velocity voxels into smaller sub-cubes before feeding them to the neural network. We take such process based on the following considerations:

- Learning a larger cube requires a larger number of neurons or layers in the network, making the training more difficult and expensive.
- Dealing with large fields is limited by memory constraints, especially if GPUs are used in the training process.
- By using small cubes as training samples, we force the neural network to focus on interpreting and predicting the small-scale, non-linear patterns in the velocity fields. The large-scale velocity field, which can be easily estimated using perturbation theory, is not our focus.

To avoid possible inaccuracy and complexity brought by the boundary effects, the neural network is designed to map the density fields into momentum fields *having a smaller size*. For each momentum field, we take a 240^3 -voxel subfield from

⁵ One small problem is that at some lattice points the value of the density is estimated to be zero. We assign them the background velocity, which equals to the mean momentum divided by the mean density.

it, cut the subfield into 1,728 20^3 -voxel subcubes, and set the subcubes as the targets (i.e. outputs) of the neural network. The inputs of the network are a series of 32^3 -voxel density fields sharing the same centers with those momentum fields. In this way, 75% voxels (lying near the outer boundary of the density fields) serve as adjacent points, for the purpose of enhancing accuracy.

Furthermore, since the density values span three orders of magnitude, it is difficult for the neural network to establish an accurate mapping. Thus we use the following logarithmic transform to mitigate this problem

$$\tilde{\rho}(x, y, z) = \ln(\rho(x, y, z) + 1). \quad (1)$$

By using their log values, we greatly decrease the variance. Moreover, the distribution of large scale structure density is close to the lognormal distribution, so we can use the above expression to convert it into an approximate normal distribution Falck et al. (2012); Neyrinck et al. (2009); Kitaura and Angulo (2012).

The 32^3 -voxel fields are split into training, verification and test sets, among which the training set accounts for 60%, the verification set accounts for 30%, and the test set accounts for 10% of the total data. The single batch number for the training is set as 6.

3. NEURAL NETWORK ARCHITECTURE

We adopt a ‘‘U-net’’ style architecture, which is built upon the Convolutional Network and modified in a way that it has better performance in imaging analysis.

As mentioned in the previous section, the entire simulation box were into 32^3 -voxel subcubes with a size of $(64 h^{-1} \text{ Mpc})^3$, and mapped into 20^3 -voxel velocity fields. $64 h^{-1} \text{ Mpc}$ is large enough to capture the non-linear features in the field, while reducing the input data complexity, thus reducing the required number of neurons. Accordingly, the overall structure of our network is designed as follows (see Figure 2),

- First, the input 32 -voxel density fields are fed into two convolution layers, which *convolve* the inputs and pass the resulting feature fields to the next-level layers. To capture the abundant features in the 3-D LSS, each layer has 128 filters, while each filter has a shape of 3^3 . The latter configuration is adopted throughout our network. These two convolution layers are designed to have zero-padding and 1-stride (in what follows ‘‘same convolution’’), so that their outputs have the same dimension to their inputs.
- Then, the feature fields are convolved by 128 3^3 -filters, but using a stride of 2. Therefore, the outputs are reduced to the size of 16^3 . In this step we use the convolution (stride=2) to effectively decrease the dimensions of the feature maps, and thus reduce the number of parameters to learn and the amount of computation performed in the network.
- To further extract features and compress them, the 16^3 -voxel feature fields are then processed by two same convolution and one convolution (stride=2), for further feature extraction and compression. Here the three layers have as many as 256 filters, as we expect more features when entering a deeper-level regime.

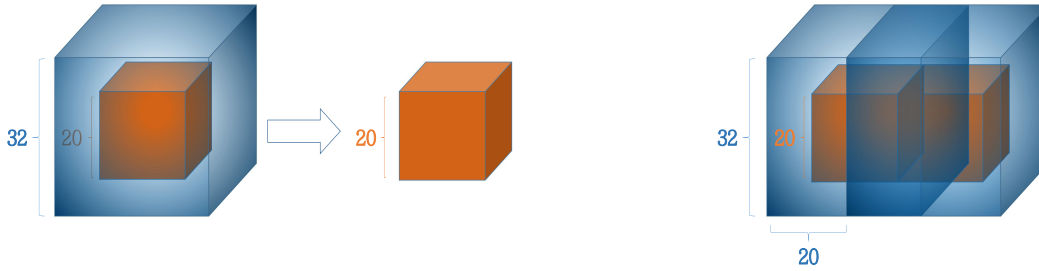


FIG. 1.— Left panel: The input of our neural network is a 32^3 -voxel density field (blue), while the output is a 20^3 -voxel velocity field (red) located around the center of the input. This choice reduces boundary effects. Right panel: A series of overlapped input fields yield to non-overlapped outputs which can be spliced back to build up larger cubes.

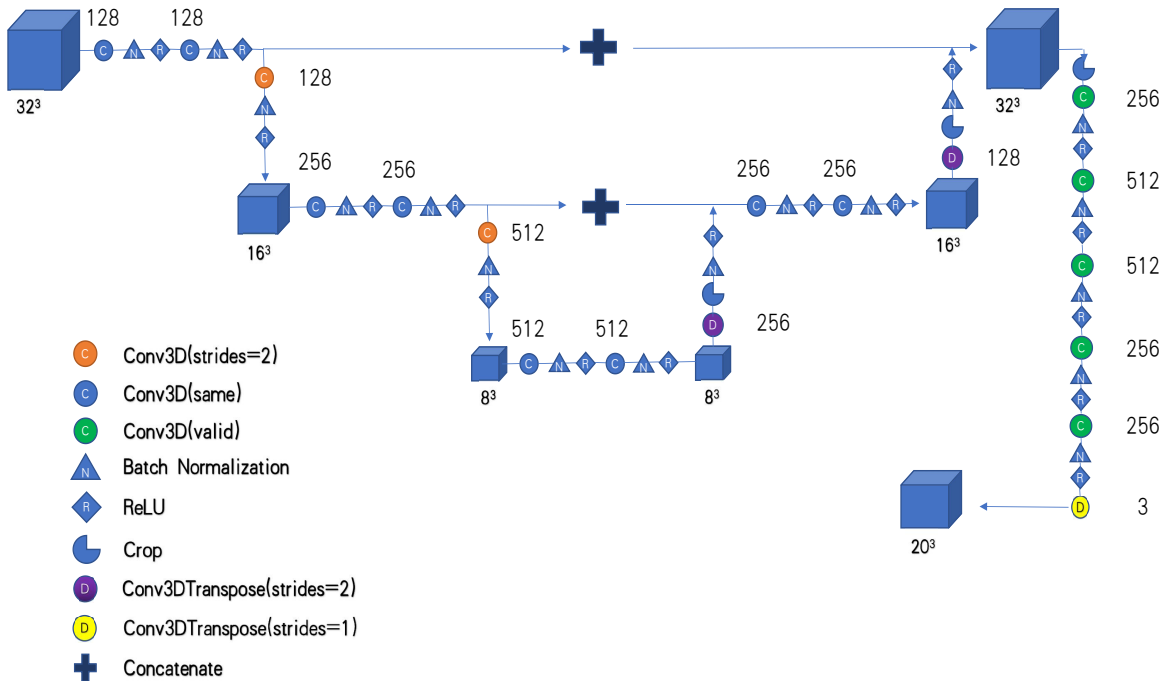


FIG. 2.— The overall structure of our network is designed similar to the “U-net” style architecture, which is built upon the Convolutional Network and modified in a way that it has better performance in imaging analysis. It is consisting of 15 convolution layers and 2 deconvolution layers, and maps the 32^3 -voxel density field ($64 h^{-1}\text{Mpc}$) to the 20^3 -voxel velocity or momentum fields ($40 h^{-1}\text{Mpc}$). A lot of detailed designs are adopted to guarantee the performance of the network.

- The outputs of the previous layers, i.e. $256 \ 8^3$ -voxel fields, are passed to two same convolution layers having $512 \ 3^3$ -filters in each, to further extracting features.
- After that, a series of deconvolution layers are placed to conduct “inverse convolution” and achieve reconstruction. The $512 \ 8^3$ -voxel fields are firstly deconvolved by $256 \ 3^3$ -filters to produce 16^3 -voxel fields, then convolved by $256 \ 3^3$ -filters for further information extraction, and finally deconvolved by $128 \ 3^3$ -filters to recover 32^3 -voxel fields. The deconvolution is achieved via transpose convolution layers⁶ with stride 1.
- Finally, the 32^3 -voxel feature fields are passed to six convolution layers without padding (in what follows “valid convolution”). In each valid convolution the 3^3 -filters decrease the size of the data by 2, so the final output has a shape of 20^3 . They are passed to a deconvolution layer with $3 \ 3^3$ -filters and stride 1 to build up a 20^3 -voxel cube with three dimensional velocity as the final output.

In summary, the network is composed of a series of convolution and deconvolution layers and have a symmetric structure. It can be generally considered as an encoder network

⁶ Transpose convolution layer is very similar to the standard convolution layers, but differs in their receptive field; an easy way to realize it is to re-

congize it as the reverse operation of the convolution layers. And one can refer to https://keras.io/api/layers/convolution_layers/convolution3d_transpose/ for more details.

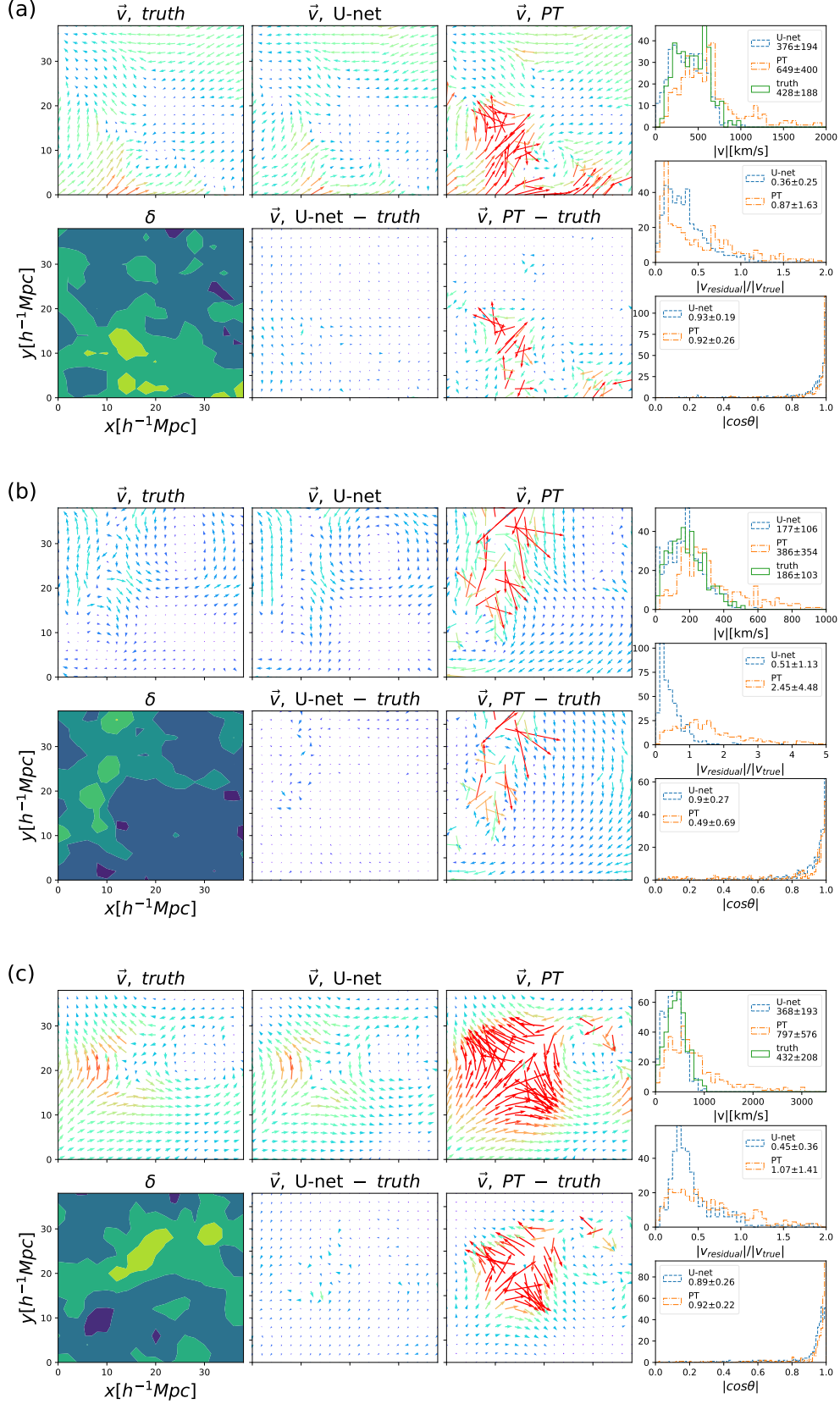
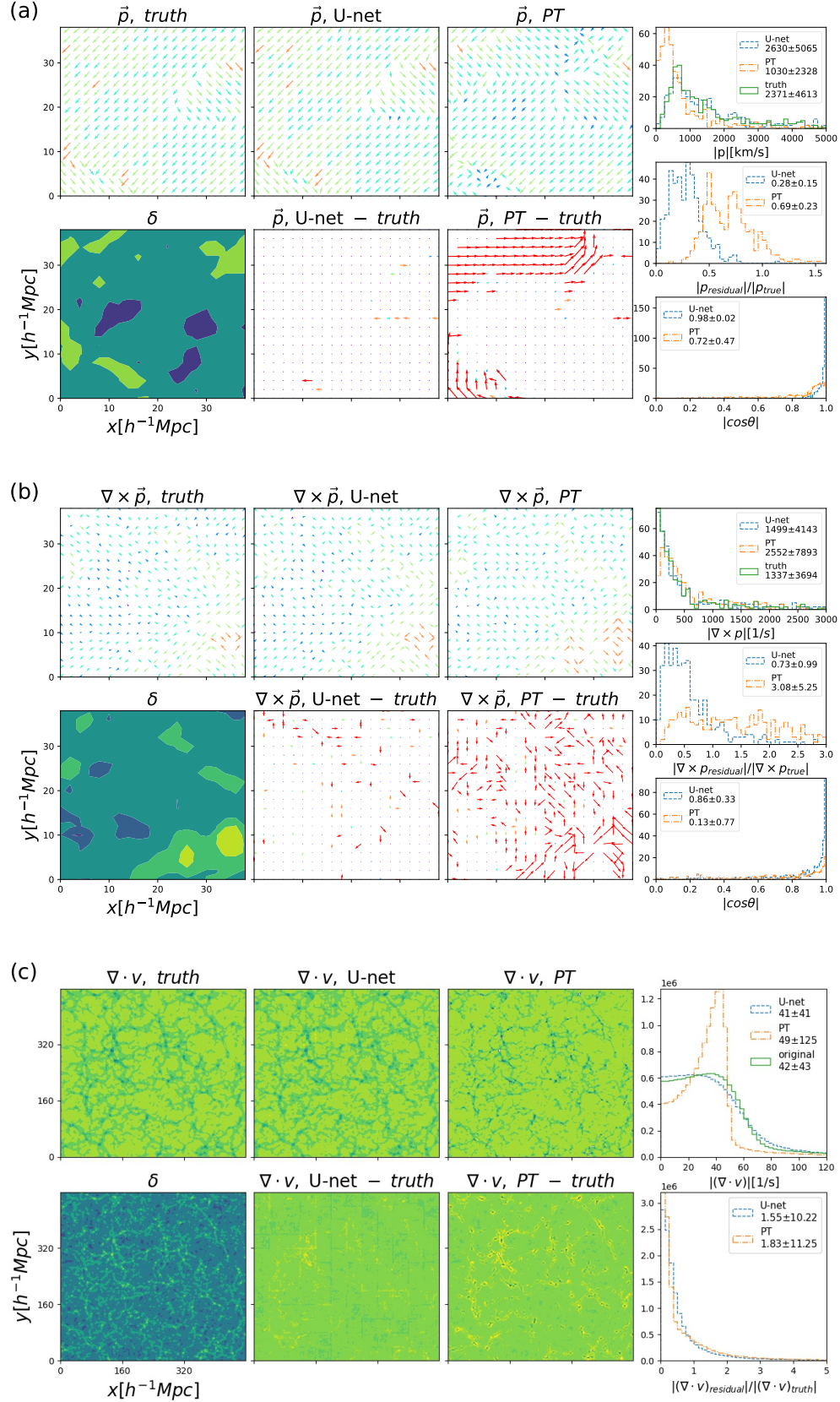


FIG. 3.— Three slices selected from the testing sample. In regions where two bulks of matter collide and merge, the velocity is highly non-linear. For each slice, We plot the velocity field of original input (top left), U-net prediction (top middle) and perturbation theory prediction (top right). In the bottom row, we also plot the corresponding density field (bottom left), residual of U-net prediction (bottom middle) and PT prediction (bottom right). In the right column, we plot the histograms of v , $|v_{\text{residual}}|/|v_{\text{true}}|$ and $|\cos\theta|$. All these suggest that the performance of neural network is much better.



followed by a decoder network. In this way, it not only identifies features at the pixel level, but projects the features learned at different stages of the encoder onto another pixel space.

A lot of detailed designs are adopted to guarantee the performance of the network. We summarize them as follows:

- In the decoder part, we adopted transpose convolution, instead of up-sampling, as the deconvolution layer. Compared with the latter design, transpose convolution does a much better job in dealing with the non-linearities in the fields. Based on the same consideration, in the encoder part, we also use transpose convolution, instead of max- or mean-pooling, to reduce the data.
- After each convolution layer we place one Batch Normalization (BN) layer and one activation layer. The former one is added to prevent the over-fitting of the model, reduce the training cost and improve the training speed. The latter one, for which we use rectified linear unit (ReLU) $f(x) = \max(x, 0)$, is crucial for the neural network, since it brings non-linearity into the system.
- Each deconvolution is followed by a cropping layer, to match the shape of the preceding encoder convolutional density field so as to meet the concatenate condition. We crop the both side with the same pixel to guarantee either side has the same weight to the velocity field.
- After every deconvolution, we *concatenate* the higher resolution feature fields from the encoder network with the deconvolved features, in order to better learn representations in the following convolutions. Since the decoder is a sparse operation, We need to fill in more details from earlier stages.
- During the training, we randomly shuffled the input training samples of each epoch to prevent the effect of overfitting due to the similarity of adjacent fields.

4. RESULT

In the following we compare the neural network outputs with the input truth and the linear perturbation theory expectations. As mentioned in the previous subsection, in order to suppress the boundary effect in the training, the output of the neural network is a 20^3 -voxel field, located in the center of the 32^3 -voxel input field. Here we have already put together those sub-cubes into a larger field (Figure 1).

4.1. Pixel-to-pixel comparison

Figure 3 shows three slices selected from the *testing* samples. They all have a size $40h^{-1} \text{ Mpc} \times 40h^{-1} \text{ Mpc}$ and a thickness $2h^{-1} \text{ Mpc}$. In all figures, we show the original “truth” velocity field, the predictions of the neural network and the linear perturbation theory, and also their residuals to the original velocity field. Plotted in the lower-left corners are the density fields based on which the velocity fields are derived.

In all cases it is clear that the neural network achieves a better performance than the linear perturbation theory:

- The linear perturbation theory works well in the regime where the density and velocity is low (e.g., see the lower-right corner of the middle and lower panels). In

the lower-right corner of the lowest panel, the performance of the perturbation theory is even better than the neural network, possibly because the latter puts most effort on predicting the non-linear regions.

- The linear perturbation theory completely fails in the non-linear regions with relatively large density and velocity. But the neural network still works well in these regions.
- The most interesting cases are those corresponding to merging situations where two regions with opposing bulk velocities collide into each other. This is shown in the lower-left part of the uppermost panel, the upper-left corner of the middle panel, and the left part of the lowest panel. While in these regions the perturbation theory completely fails, the neural network still works well in reconstructing the velocities.

To quantify the performance of the neural network, for all slices we plot the corresponding histograms of $|v|$, $|v_{\text{residual}}|/|v_{\text{true}}|$, and $\cos\theta$, where θ is the angle between the original and the predicted velocities.

We find the neural network correctly recovers the distribution of $|v|$. However the linear perturbation theory tends to over-predict the velocity in the dense regions. In the three slices, when checking the distribution of $|v|$, the original fields give

$$|v| = 428 \pm 188, 186 \pm 103, 432 \pm 208 \text{ km/s (original),} \quad (2)$$

while the neural network predictions give

$$|v| = 376 \pm 194, 177 \pm 106, 368 \pm 193 \text{ km/s (U-net),} \quad (3)$$

In comparison, the linear perturbation theory predictions are

$$|v| = 649 \pm 400, 386 \pm 354, 797 \pm 576 \text{ km/s (PT).} \quad (4)$$

Comparing $|v_{\text{residual}}|$, the neural network results are

$$|v_{\text{residual}}| = 126 \pm 72, 65 \pm 41, 152 \pm 70 \text{ km/s (U-net)} \quad (5)$$

while the linear perturbation theory yields

$$|v_{\text{residual}}| = 281 \pm 349, 298 \pm 299, 407 \pm 488 \text{ km/s (PT)} \quad (6)$$

The latter results are much worse. The residual velocities of the neural network results are 3–4 times smaller than the linear perturbation theory results.

Finally, the neural network performs better than linear theory in predicting the directions of the flows. They have $|\cos\theta| = 0.93 \pm 0.19, 0.9 \pm 0.27, 0.89 \pm 0.26$ for the three slices, while in the case of linear perturbation theory the results are $0.92 \pm 0.26, 0.49 \pm 0.69, 0.92 \pm 0.22$. The neural network results are closer to 1 and with a smaller standard deviation.

Similar result can be seen in Fig.4. In the non-linear regime, linear perturbation theory completely fails, while the U-net architecture can still correctly recover the momentum. When checking the distribution of $|p|$, the original fields give

$$|p| = 2371 \pm 4613 \text{ km/s (original),} \quad (7)$$

while the neural network predictions give

$$|p| = 2415 \pm 4361 \text{ km/s (U-net),} \quad (8)$$

In comparison, the linear perturbation theory predictions are

$$|p| = 1030 \pm 2318 \text{ km/s (PT).} \quad (9)$$

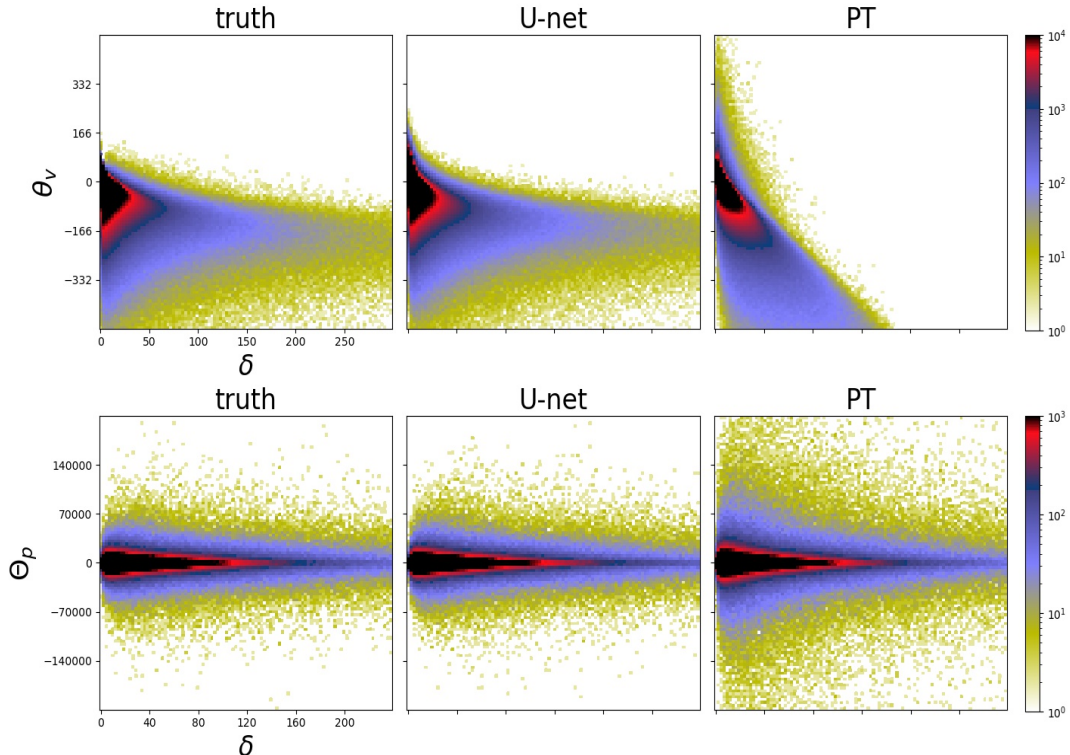


FIG. 5.— Distribution of the velocity divergence θ_v , and the x-direction momentum curl Θ_p , along with the density contrast δ . From left to right, we show the results calculated using the truth field and the fields predicted by the U-net and PT methods, in a $480 h^{-1}\text{Mpc}$ box with cell-size $2 h^{-1}\text{Mpc}$.

In the middle panel, we show that the neural network also performs much better in reconstructing the curl of the momentum field.

Another important quantity to characterize is the divergence of the velocity field, given its relevance to study superclusters and the cosmic web Hoffman et al. (2012); Peñaranda-Rivera et al. (2020). So we analyze the divergence of the velocity field predicted by the neural network and compare it with the linear perturbation theory. We find again that the neural network outperforms linear perturbation theory. In Fig.4, the divergence of velocity field predicted by the neural network is similar to the real one, while the linear perturbation theory has a larger variance.

In addition, we also made a cell-to-cell comparison of the $\delta\text{-}\theta_v$ and $\delta\text{-}\Theta_p$ distribution of the truth field and the U-net or PT predicted fields, in a $480 h^{-1}\text{Mpc}$ box with cell-size $2h^{-1}\text{Mpc}$. Figure 5 shows that, the scattering pattern of the U-net predicted field is basically consistent with that of the truth field. In comparison, the PT method leads to a significantly wrong $\delta\text{-}\theta_v$ distribution, and also seriously overpredicts the curl value of many cells.

4.2. Power Spectrum

We now proceed to check the clustering properties of the fields. The most commonly used statistics in cosmological studies are the two-point correlation function measured in configuration space, or the power spectrum measured in Fourier space. In what follows, we compute the two-point correlation function and power spectra of specific quantities defined as

$$\begin{aligned} \xi_{AA}(|r|) &= \langle \delta_A(r') \delta_A(r'+r) \rangle \\ P_{AA}(|k|) &= \int d^3r \xi(r) e^{ik \cdot r} \end{aligned} \quad (10)$$

, where the angle bracket represents the average of the whole sample, and A denotes the physical quantities we choose to investigate. In this analysis, the following power spectrum are taken into account,

$$P_{|v||v|}, P_{\theta_v}, P_{pp}, P_{\Theta_p, \Theta_p} \quad (11)$$

where $|v| = \sqrt{v_x^2 + v_y^2 + v_z^2}$, $\theta_v \equiv \nabla \cdot \mathbf{v}$, $p = |v|\delta$ is the momentum and $\Theta_p \equiv \nabla \times \mathbf{p}$. In order to compare the difference between the reconstructed field and the actual field, we define

$$T(k) = \frac{P_{\text{predicted}}(k)}{P_{\text{true}}(k)} \quad (12)$$

to characterize the difference between the reconstructed and true fields. All measures are conducted in $(120h^{-1}\text{Mpc})^3$ -boxes constructed from the testing samples.

Figure 6 shows the $P_{|v||v|}, P_{\theta_v}, P_{pp}, P_{\Theta_p, \Theta_p}$ of U-net and PT methods and their residuals to the actual power spectrum. Table 1234 compares the ratio of the power spectrum of PT and U-Net in different physical quantities mentioned above to the real power spectrum at $k = 0.2, 0.6$ and 1.0 . When checking the results of $P_{|v||v|}$, the neural network much better recover its value in the quasi non-linear regime of $k \gtrsim 0.2 h\text{Mpc}^{-1}$. In particular, we find $\lesssim 20\%$ discrepancy in $P_{|v||v|}$ within the range of $0.2 h\text{Mpc}^{-1} \lesssim k \lesssim 1.4 h\text{Mpc}^{-1}$. The largest discrepancy occurs at $k \simeq 0.272 h\text{Mpc}^{-1}$, corresponding to a $T(k)$ of 0.801. In contrast, the perturbation theory result always has a discrepancy of $T(k) \simeq 1.8\text{--}5.3$.

Similar results are found when comparing the other two power spectra. In P_{pp} we find a $\lesssim 8.2\%$ discrepancy within the range of $0.2 h\text{Mpc}^{-1} \lesssim k \lesssim 1.4 h\text{Mpc}^{-1}$. The largest discrepancy, at $k \simeq 0.816 h\text{Mpc}^{-1}$, corresponds to a $T(k)$ of 0.918,

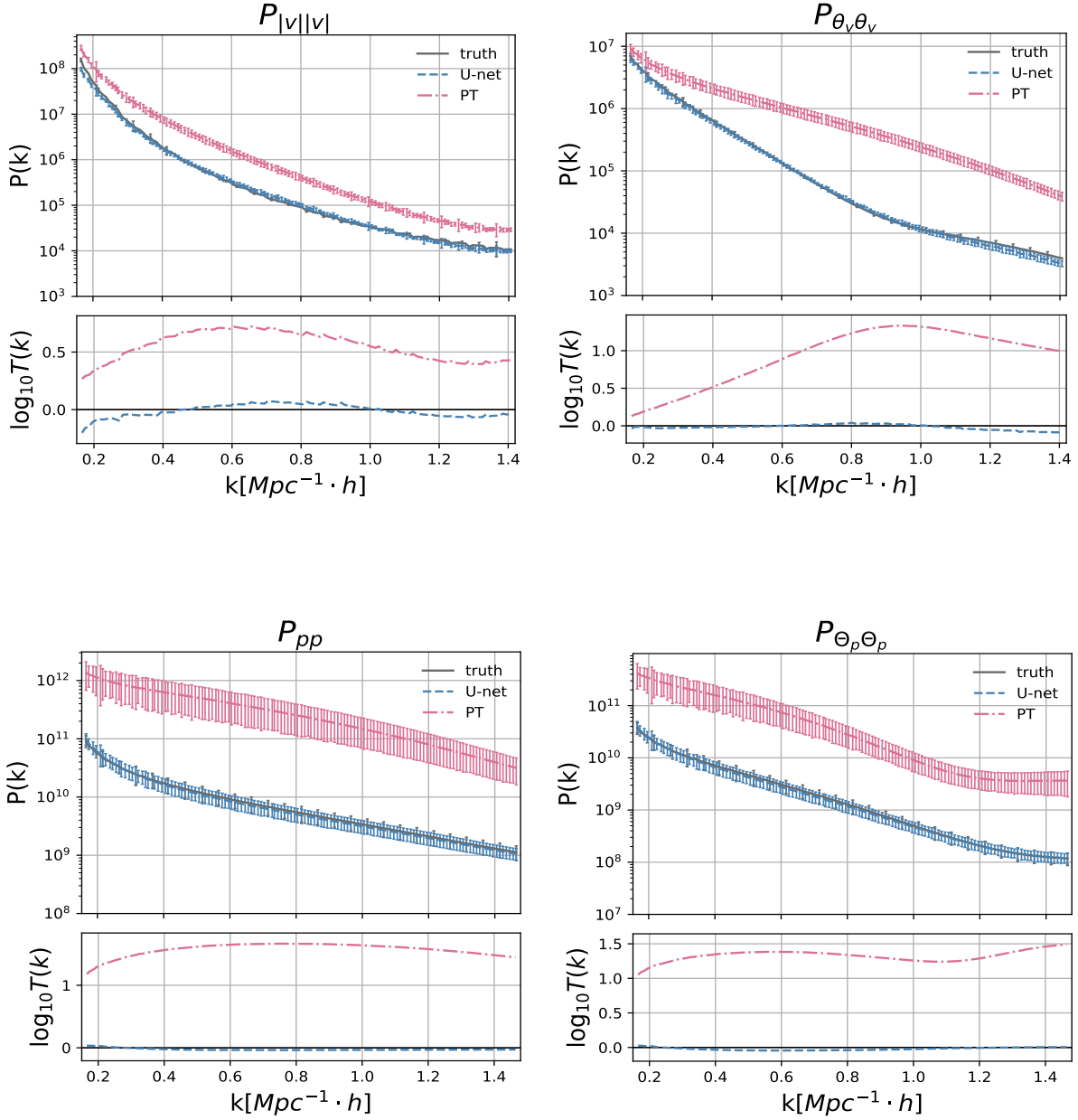


FIG. 6.— The quantities $P_{|v||v|}$, $P_{\theta_v\theta_v}$, P_{pp} , $P_{\Theta_p\Theta_p}$ are computed in 64 boxes with the size of $120^3 h^{-1} \text{Mpc}^3$. The gray line, blue line, and pink line represent the real field, U-net prediction field, and the linear perturbation theory field, respectively. The U-net prediction power spectrum performs much better than linear perturbation theory. The bottom figures show the deviation of the predicted power spectrum to real field. The y axis $\log_{10} T$ is defined as $\log_{10} P_{\text{predicted}}/P_{\text{true}}$. All the figures within the range of $0.2 \lesssim k \lesssim 1.5$ show the U-net prediction approximates 0 while the linear perturbation theory has great deviation.

while the perturbation theory result always has a discrepancy of $T(k) \simeq 15-47$.

We find $\lesssim 18\%$ discrepancy in $P_{\theta_v\theta_v}$, within the range of $0.2 h\text{Mpc}^{-1} \lesssim k \lesssim 1.4 h\text{Mpc}^{-1}$. The largest discrepancy, at $k \simeq 1.335 h\text{Mpc}^{-1}$, corresponds to a $T(k)$ of 0.818, while perturbation theory consistently exhibits a discrepancy of $T(k) \simeq 1.3-22$.

There is a discrepancy of $\lesssim 9.2\%$ in $P_{\Theta_p\Theta_p}$, within the range of $0.2 h\text{Mpc}^{-1} \lesssim k \lesssim 1.4 h\text{Mpc}^{-1}$. The largest discrepancy is

seen at $k \simeq 0.604 h\text{Mpc}^{-1}$ with a $T(k)$ value of 0.907, while perturbation theory has a discrepancy of $T(k) \simeq 11-31$.

It is worth noting here that since the outputs of our U-net only have a size of $40 h^{-1} \text{Mpc}$, the sampling spatial sampling limits our ability to accurately recover the large-scale power spectra at $k < 0.2 h\text{Mpc}^{-1}$. This can be improved by making corrections on large scales, or simply increase the sizes of the input or output fields. Since the major focus of this work is to check the capability of the neural network in predicting small-scale, non-linear velocity fields, we will not discuss this issue

TABLE 1
VALUES OF $P_{|v||v|}/P_{\text{true}}$, SAMPLED AT $k = 0.2, 0.6$ AND 1.0

k ($h\text{Mpc}^{-1}$)	0.2	0.6	1.0
$P_{ v v }/P_{\text{true}}$, linear perturbation theory	2.259	5.245	3.516
$P_{ v v }/P_{\text{true}}$, U-net	0.818	1.123	1.011

TABLE 2
VALUES OF P_{pp}/P_{true} , SAMPLED AT $k = 0.2, 0.6$ AND 1.0

k ($h\text{Mpc}^{-1}$)	0.2	0.6	1.0
P_{pp}/P_{true} , linear perturbation theory	20.860	44.746	43.479
P_{pp}/P_{true} , U-net	1.068	0.920	0.929

TABLE 3
VALUES OF $P_{\theta_v}/P_{\text{true}}$, SAMPLED AT $k = 0.2, 0.6$ AND 1.0

k ($h\text{Mpc}^{-1}$)	0.2	0.6	1.0
$P_{\theta_v}/P_{\text{true}}$, linear perturbation theory	1.584	7.917	20.731
$P_{\theta_v}/P_{\text{true}}$, U-net	0.956	0.996	1.011

TABLE 4
VALUES OF $P_{\Theta_p\Theta_p}/P_{\text{true}}$, SAMPLED AT $k = 0.2, 0.6$ AND 1.0

k ($h\text{Mpc}^{-1}$)	0.2	0.6	1.0
$P_{\Theta_p\Theta_p}/P_{\text{true}}$, linear perturbation theory	14.806	24.086	18.065
$P_{\Theta_p\Theta_p}/P_{\text{true}}$, U-net	1.048	0.907	0.95

in details.

5. DISCUSSION AND CONCLUSIONS

In this paper, we applied a deep learning technique to reconstruct the velocity field from the dark matter density field, which has a resolution of $2 h^{-1}\text{Mpc}$. To this end we implement a ‘‘U-net’’ neural network, consisting of 15 convolution layers and 2 deconvolution layers with 48,690,307 parameters. The network maps the 32^3 -voxel input density field to velocity and momentum fields having size of 20^3 , so as to avoid boundary effects.

We find that the neural network manages to reconstruct the velocity and momentum fields and even outperforms the results from linear perturbation theory. The superiority of the neural network is more pronounced in regions where the density is relatively large and the non-linear processes dominate. In particular, in regions where mergers take place, linear perturbation theory completely fails, while the neural network successfully recovers the velocity structure.

By conducting pixel-to-pixel comparison between the predicted velocity fields and underlying true fields, we find that

the neural network can reasonably recover the distribution of $|v|$, having discrepancy of $|v_{\text{residual}}| \lesssim 150$ km/s, while for the perturbation theory results we find $|v_{\text{residual}}| \simeq 300\text{--}400$ km/s. The neural network also predicts well the directions of the velocities compared to the true velocities.

When analyzing the clustering properties of the fields, the neural network can well recover the amplitude and shape of $P_{|v||v|}$, whose error ranges from 1% to $\lesssim 10\%$ within the range of $0.2 \lesssim k \lesssim 1.5$. Similarly, the error of P_{pp} is $\lesssim 8.2\%$, P_{θ_v} is $\lesssim 17\%$ and $P_{\Theta_p\Theta_p}$ is $\lesssim 9.2\%$ at the range of $0.2 \lesssim k \lesssim 1.4$. All these results are much better than the linear perturbation theory results.

As a proof-of-concept study, our analysis demonstrates the ability of deep neural networks to reconstruct the nonlinear velocity and momentum fields from density fields. The neural network can even handle regions of shell-crossing, which is notoriously difficult within perturbation theory approaches. At the same time, there is still much room for improvement in the accuracy of the neural network, via further optimizing the architecture, enlarging the number of the training samples, or adding follow-up neural networks to fit the residuals and do corrections.

The reconstructed peculiar velocity fields can be used for a number of studies, such as BAO reconstructions, RSD analyses, kinematic Sunyaev-Zeldovich (kSZ), supercluster analysis and the cosmic web construction. We will continue to work on this direction so that the machine learning technique can be reliably applied to real observational data and help us uncover more of the mysteries of the universe.

We thank Kwan-Chuen Chan, Yin Li, Jie Wang, Le Zhang and Yi Zheng for helpful discussions. This work is supported by National SKA Program of China No. 2020SKA0110401. XDL acknowledges the support from the NSFC grant (No. 11803094) and the Science and Technology Program of Guangzhou, China (No. 202002030360). CGS acknowledges financial support from the National Research Foundation of Korea (NRF; #2020R111A1A01073494). J.E. F-R acknowledges support from COLCIENCIAS Contract No. 287-2016, Project 1204-712-50459. Y.W. is supported by NSFC grant No.11803095 and NSFC grant No.11733010. We acknowledge the use of Tianhe-2 supercomputer. We also acknowledge the use of the Kunlun cluster, a supercomputer owned by the School of Physics and Astronomy, Sun Yat-Sen University.

REFERENCES

- N. Kaiser, *MNRAS* **227**, 1 (1987).
 J. Jackson, *Monthly Notices of the Royal Astronomical Society* **156**, 1P (1972).
 D. J. Eisenstein, I. Zehavi, D. W. Hogg, R. Scoccimarro, M. R. Blanton, R. C. Nichol, R. Scranton, H.-J. Seo, M. Tegmark, Z. Zheng, S. F. Anderson, J. Annis, N. Bahcall, J. Brinkmann, S. Burles, F. J. Castander, A. Connolly, I. Csabai, M. Doi, M. Fukugita, J. A. Frieman, K. Glazebrook, J. E. Gunn, J. S. Hendry, G. Hennessy, Z. Ivezić, S. Kent, G. R. Knapp, H. Lin, Y.-S. Loh, R. H. Lupton, B. Margon, T. A. McKay, A. Meiksin, J. A. Munn, A. Pope, M. W. Richmond, D. Schlegel, D. P. Schneider, K. Shimasaku, C. Stoughton, M. A. Strauss, M. SubbaRao, A. S. Szalay, I. Szapudi, D. L. Tucker, B. Yanny, and D. G. York, *ApJ* **633**, 560 (2005), astro-ph/0501171.
 D. J. Eisenstein, H.-J. Seo, E. Sirko, and D. N. Spergel, *ApJ* **664**, 675 (2007), arXiv:astro-ph/0604362 [astro-ph].
 C. Alcock and B. Paczyński, *Nature* **281**, 358 (1979).
 X.-D. Li, C. Park, J. E. Forero-Romero, and J. Kim, *ApJ* **796**, 137 (2014), arXiv:1412.3564.
 X.-D. Li, C. Park, C. G. Sabiu, and J. Kim, *Monthly Notices of the Royal Astronomical Society* **450**, 807 (2015).
 X.-D. Li, C. Park, C. G. Sabiu, H. Park, D. H. Weinberg, D. P. Schneider, J. Kim, and S. E. Hong, *ApJ* **832**, 103 (2016), arXiv:1609.05476 [astro-ph.CO].
 D. K. Ramanah, G. Lavaux, J. Jasche, and B. D. Wandelt, *A&A* **621**, A69 (2019), arXiv:1808.07496.
 J. M. Bardeen, J. R. Bond, N. Kaiser, and A. S. Szalay, *ApJ* **304**, 15 (1986).
 O. Hahn, C. Porciani, C. M. Carollo, and A. Dekel, *Monthly Notices of the Royal Astronomical Society* **375**, 489 (2007).
 J. Forero-Romero, Y. Hoffman, S. Gottlöber, A. Klypin, and G. Yepes, *Monthly Notices of the Royal Astronomical Society* **396**, 1815 (2009).
 Y. Hoffman, O. Metuki, G. Yepes, S. Gottlöber, J. E. Forero-Romero, N. I. Libeskind, and A. Knebe, *Monthly Notices of the Royal Astronomical Society* **425**, 2049 (2012).

- J. E. Forero-Romero, S. Contreras, and N. Padilla, *Monthly Notices of the Royal Astronomical Society* **443**, 1090 (2014).
- F. Fang, J. Forero-Romero, G. Rossi, X.-D. Li, and L.-L. Feng, *MNRAS* **485**, 5276 (2019), arXiv:1809.00438 [astro-ph.CO].
- R. A. Sunyaev and Y. B. Zeldovich, *Comments on Astrophysics and Space Physics* **4**, 173 (1972).
- R. A. Sunyaev and Y. B. Zeldovich, *MNRAS* **190**, 413 (1980).
- R. K. Sachs and A. M. Wolfe, *ApJ* **147**, 73 (1967).
- M. J. Rees and D. W. Sciama, *Nature* **217**, 511 (1968).
- R. G. Crittenden and N. Turok, *Phys. Rev. Lett.* **76**, 575 (1996), arXiv:astro-ph/9510072 [astro-ph].
- M. M. Phillips, *ApJ* **413**, L105 (1993).
- A. G. Riess, M. Davis, J. Baker, and R. P. Kirshner, *ApJ* **488**, L1 (1997), arXiv:astro-ph/9707261 [astro-ph].
- D. J. Radburn-Smith, J. R. Lucey, and M. J. Hudson, *MNRAS* **355**, 1378 (2004), arXiv:astro-ph/0409551 [astro-ph].
- S. J. Turnbull, M. J. Hudson, H. A. Feldman, M. Hicken, R. P. Kirshner, and R. Watkins, *MNRAS* **420**, 447 (2012), arXiv:1111.0631 [astro-ph.CO].
- G. J. Mathews, B. M. Rose, P. M. Garnavich, D. G. Yamazaki, and T. Kajino, *ApJ* **827**, 60 (2016), arXiv:1412.1529 [astro-ph.CO].
- R. B. Tully and J. R. Fisher, *A&A* **500**, 105 (1977).
- K. L. Masters, C. M. Springob, M. P. Haynes, and R. Giovanelli, *ApJ* **653**, 861 (2006), arXiv:astro-ph/0609249 [astro-ph].
- K. L. Masters, C. M. Springob, and J. P. Huchra, *AJ* **135**, 1738 (2008), arXiv:0711.4305 [astro-ph].
- A. Dressler, D. Lynden-Bell, D. Burstein, R. L. Davies, S. M. Faber, R. Terlevich, and G. Wegner, *ApJ* **313**, 42 (1987).
- S. Djorgovski and M. Davis, *ApJ* **313**, 59 (1987).
- C. M. Springob, K. L. Masters, M. P. Haynes, R. Giovanelli, and C. Marinoni, *ApJS* **172**, 599 (2007).
- A. Nusser, A. Dekel, E. Bertschinger, and G. R. Blumenthal, *ApJ* **379**, 6 (1991).
- F. Bernardeau, *ApJ* **390**, L61 (1992).
- S. Zaroubi, Y. Hoffman, K. B. Fisher, and O. Lahav, *ApJ* **449**, 446 (1995), arXiv:astro-ph/9410080 [astro-ph].
- R. A. C. Croft and E. Gaztanaga, *MNRAS* **285**, 793 (1997), arXiv:astro-ph/9602100 [astro-ph].
- F. Bernardeau, M. J. Chodorowski, E. L. Łokas, R. Stompor, and A. Kudlicki, *MNRAS* **309**, 543 (1999), arXiv:astro-ph/9901057 [astro-ph].
- A. Kudlicki, M. Chodorowski, T. Plewa, and M. Różycka, *MNRAS* **316**, 464 (2000), arXiv:astro-ph/9910018 [astro-ph].
- E. Branchini, A. Eldar, and A. Nusser, *MNRAS* **335**, 53 (2002), arXiv:astro-ph/0110618 [astro-ph].
- R. Mohayaee and R. B. Tully, *ApJ* **635**, L113 (2005), arXiv:astro-ph/0509313 [astro-ph].
- G. Lavaux, R. Mohayaee, S. Colombi, R. B. Tully, F. Bernardeau, and J. Silk, *MNRAS* **383**, 1292 (2008), arXiv:0707.3483 [astro-ph].
- M. Bilicki and M. J. Chodorowski, *MNRAS* **391**, 1796 (2008), arXiv:0809.3513 [astro-ph].
- F.-S. Kitaura, R. E. Angulo, Y. Hoffman, and S. Gottlöber, *MNRAS* **425**, 2422 (2012), arXiv:1111.6629 [astro-ph.CO].
- H. Wang, H. J. Mo, X. Yang, and F. C. van den Bosch, *MNRAS* **420**, 1809 (2012), arXiv:1108.1008 [astro-ph.CO].
- E. Jennings and D. Jennings, *MNRAS* **449**, 3407 (2015), arXiv:1502.02052 [astro-ph.CO].
- M. Ata, F.-S. Kitaura, C.-H. Chuang, S. Rodríguez-Torres, R. E. Angulo, S. Ferraro, H. Gil-Marín, P. McDonald, C. Hernández Monteagudo, V. Müller, G. Yepes, M. Autfage, F. Baumgarten, F. Beutler, J. R. Brownstein, A. Burden, D. J. Eisenstein, H. Guo, S. Ho, C. McBride, M. Neyrinck, M. D. Olmstead, N. Padmanabhan, W. J. Percival, F. Prada, G. Rossi, A. G. Sánchez, D. Schlegel, D. P. Schneider, H.-J. Seo, A. Streblyanska, J. Tinker, R. Tojeiro, and M. Vargas-Magana, *MNRAS* **467**, 3993 (2017), arXiv:1605.09745 [astro-ph.CO].
- J. Schmelzle, A. Lucchi, T. Kacprzak, A. Amara, R. Sgier, A. Réfrégier, and T. Hofmann, (2017), arXiv:1707.05167 [astro-ph.CO].
- A. Gupta, J. M. Z. Matilla, D. Hsu, and Z. Haiman, *Phys. Rev.* **D97**, 103515 (2018), arXiv:1802.01212 [astro-ph.CO].
- O. M. Springer, E. O. Ofek, Y. Weiss, and J. Merten, (2018), arXiv:1808.07491 [astro-ph.CO].
- J. Fluri, T. Kacprzak, A. Lucchi, A. Refregier, A. Amara, T. Hofmann, and A. Schneider, (2019), arXiv:1906.03156 [astro-ph.CO].
- N. Jeffrey, F. Lanusse, O. Lahav, and J.-L. Starck, (2019), arXiv:1908.00543 [astro-ph.CO].
- J. Merten, C. Giocoli, M. Baldi, M. Meneghetti, A. Peel, F. Lalande, J.-L. Starck, and V. Pettorino, *Mon. Not. Roy. Astron. Soc.* **487**, 104 (2019), arXiv:1810.11027 [astro-ph.CO].
- A. Peel, F. Lalande, J.-L. Starck, V. Pettorino, J. Merten, C. Giocoli, M. Meneghetti, and M. Baldi, *Phys. Rev.* **D100**, 023508 (2019), arXiv:1810.11030 [astro-ph.CO].
- M. Tewes, T. Kuntzer, R. Nakajima, F. Courbin, H. Hildebrandt, and T. Schrabback, *Astron. Astrophys.* **621**, A36 (2019), arXiv:1807.02120 [astro-ph.CO].
- J. Caldeira, W. L. K. Wu, B. Nord, C. Avestruz, S. Trivedi, and K. T. Story, (2018), 10.1016/j.ascom.2019.100307, arXiv:1810.01483 [astro-ph.CO].
- A. C. Rodriguez, T. Kacprzak, A. Lucchi, A. Amara, R. Sgier, J. Fluri, T. Hofmann, and A. Réfrégier, *Comput. Astrophys. Cosmol.* **5**, 4 (2018), arXiv:1801.09070 [astro-ph.CO].
- N. Perraudin, M. Defferrard, T. Kacprzak, and R. Sgier, *Astron. Comput.* **27**, 130 (2019), arXiv:1810.12186 [astro-ph.CO].
- M. Münchmeyer and K. M. Smith, (2019), arXiv:1905.05846 [astro-ph.CO].
- A. Mishra, P. Reddy, and R. Nigam, (2019), arXiv:1908.04682 [astro-ph.CO].
- S. Ravanbakhsh, J. Oliva, S. Fromenteau, L. C. Price, S. Ho, J. Schneider, and B. Póczos, (2017), arXiv:1711.02033 [astro-ph.CO].
- L. Lucie-Smith, H. V. Peiris, A. Pontzen, and M. Lochner, *Mon. Not. Roy. Astron. Soc.* **479**, 3405 (2018), arXiv:1802.04271 [astro-ph.CO].
- C. Modi, Y. Feng, and U. Seljak, *JCAP* **1810**, 028 (2018), arXiv:1805.02247 [astro-ph.CO].
- P. Berger and G. Stein, *Mon. Not. Roy. Astron. Soc.* **482**, 2861 (2019), arXiv:1805.04537 [astro-ph.CO].
- S. He, Y. Li, Y. Feng, S. Ho, S. Ravanbakhsh, W. Chen, and B. Póczos, *Proc. Nat. Acad. Sci.* **116**, 13825 (2019), arXiv:1811.06533 [astro-ph.CO].
- L. Lucie-Smith, H. V. Peiris, and A. Pontzen, (2019), arXiv:1906.06339 [astro-ph.CO].
- D. N. Pfeffer, P. C. Breysse, and G. Stein, (2019), arXiv:1905.10376 [astro-ph.CO].
- D. K. Ramanah, T. Charnock, and G. Lavaux, *Phys. Rev.* **D100**, 043515 (2019), arXiv:1903.10524 [astro-ph.CO].
- T. Tröster, C. Ferguson, J. Harnois-Déraps, and I. G. McCarthy, *Mon. Not. Roy. Astron. Soc.* **487**, L24 (2019), arXiv:1903.12173 [astro-ph.CO].
- X. Zhang, Y. Wang, W. Zhang, Y. Sun, S. He, G. Contardo, F. Villaescusa-Navarro, and S. Ho, (2019), arXiv:1902.05965 [astro-ph.CO].
- T.-X. Mao, J. Wang, B. Li, Y.-C. Cai, B. Falck, M. Neyrinck, and A. Szalay, arXiv e-prints, arXiv:2002.10218 (2020), arXiv:2002.10218 [astro-ph.CO].
- S. Pan, M. Liu, J. Forero-Romero, C. G. Sabiu, Z. Li, H. Miao, and X.-D. Li, *Science China Physics, Mechanics, and Astronomy* **63**, 110412 (2020), arXiv:1908.10590 [astro-ph.CO].
- C. Dreissigacker, R. Sharma, C. Messinger, R. Zhao, and R. Prix, *Phys. Rev.* **D100**, 044009 (2019), arXiv:1904.13291 [gr-qc].
- T. D. Gebhard, N. Kilbertus, I. Harry, and B. Schölkopf (2019) arXiv:1904.08693 [astro-ph.IM].
- P. La Plante and M. Ntampaka, *Astrophys. J.* **810**, 110 (2018), arXiv:1810.08211 [astro-ph.CO].
- N. Gillet, A. Mesinger, B. Greig, A. Liu, and G. Ucci, *Mon. Not. Roy. Astron. Soc.* **484**, 282 (2019), arXiv:1805.02699 [astro-ph.CO].
- S. Hassan, A. Liu, S. Kohn, and P. La Plante, *Mon. Not. Roy. Astron. Soc.* **483**, 2524 (2019a), arXiv:1807.03317 [astro-ph.CO].
- J. Chardin, G. Uhlrich, D. Aubert, N. Deparis, N. Gillet, P. Ocvirk, and J. Lewis, (2019), arXiv:1905.06958 [astro-ph.CO].
- S. Hassan, S. Andrianomena, and C. Doughty, (2019b), arXiv:1907.07787 [astro-ph.CO].
- M. Lochner, J. D. McEwen, H. V. Peiris, O. Lahav, and M. K. Winter, *Astrophys. J. Suppl.* **225**, 31 (2016), arXiv:1603.00882 [astro-ph.IM].
- A. Moss, (2018), arXiv:1810.06441 [astro-ph.IM].
- E. E. O. Ishida et al. (COIN), *Mon. Not. Roy. Astron. Soc.* **483**, 2 (2019), arXiv:1804.03765 [astro-ph.IM].
- S.-Y. Li, Y.-L. Li, and T.-J. Zhang, (2019), arXiv:1907.00568 [astro-ph.CO].
- D. Muthukrishna, D. Parkinson, and B. Tucker, (2019), arXiv:1903.02557 [astro-ph.IM].
- P. Mehta, M. Bukov, C.-H. Wang, A. G. R. Day, C. Richardson, C. K. Fisher, and D. J. Schwab, *Phys. Rept.* **810**, 1 (2019), arXiv:1803.08823 [physics.comp-ph].
- W. D. Jennings, C. A. Watkinson, F. B. Abdalla, and J. D. McEwen, *Mon. Not. Roy. Astron. Soc.* **483**, 2907 (2019), arXiv:1811.09141 [astro-ph.CO].
- G. Carleo, I. Cirac, K. Cranmer, L. Daudet, M. Schuld, N. Tishby, L. Vogt-Maranto, and L. Zdeborová, (2019), arXiv:1903.10563 [physics.comp-ph].
- M. Ntampaka et al., (2019), arXiv:1902.10159 [astro-ph.IM].
- S. Tassev, M. Zaldarriaga, and D. J. Eisenstein, *J. Cosmology Astropart. Phys.* **2013**, 036 (2013), arXiv:1301.0322 [astro-ph.CO].
- B. L. Falck, M. C. Neyrinck, M. A. Aragon-Calvo, G. Lavaux, and A. S. Szalay, *ApJ* **745**, 17 (2012), arXiv:1111.4466 [astro-ph.CO].
- M. C. Neyrinck, I. Szapudi, and A. S. Szalay, *ApJ* **698**, L90 (2009), arXiv:0903.4693 [astro-ph.CO].
- F.-S. Kitaura and R. E. Angulo, *MNRAS* **425**, 2443 (2012), arXiv:1111.6617 [astro-ph.CO].
- Y. Hoffman, O. Metuki, G. Yepes, S. Gottlöber, J. E. Forero-Romero, N. I. Libeskind, and A. Knebe, *MNRAS* **425**, 2049 (2012), arXiv:1201.3367 [astro-ph.CO].
- J. D. Peñaranda-Rivera, D. L. Paipa-León, S. D. Hernández-Charpak, and J. E. Forero-Romero, *MNRAS* (2020), 10.1093/mnras/laaa177, arXiv:2010.05160 [astro-ph.CO].